Low frequency ultrasonic guided wave propagation through honeycomb sandwich structures with non-uniform core thickness

Aurovinda Kumar Mitra [a], Aparna A. Aradhye [b], Dhanashri M. Joglekar [a,*]

[a] *Department of Mechanical and Industrial Engineering, Indian Institute of Technology Roorkee, 247667, India*
[b] *Structural Integrity Division, CSIR-National Aerospace Laboratories (CSIR-NAL), Bengaluru 560017, Karnataka, India*

ARTICLE INFO

ABSTRACT

Honeycomb core sandwich structures (HCSSs) are used prevalently in the aerospace and marine industries. Use of guided wave-based inspections has attracted much attention in the recent past for facilitating the NDE of such structures. This paper presents the numerical and experimental analyses of the guided wave propagation through a tapered HCSS, with a primary motive to comprehend and further utilize the alteration of local wave properties as a function of the varying thickness. To this end, a low frequency fundamental antisymmetric mode is used as an interrogation signal. The numerical analysis is performed using 3D finite element simulations, while the experiments are performed on the portion of a helicopter blade with GFRP face sheets and aluminium core. The generation of the global guided waves (GGWs) as well as continuous variation of the local wave properties (wavenumber, group velocity, and phase speed) are ascertained both numerically as well as experimentally. Least-square polynomial fits are presented for the variation of group velocity along the propagation direction. A method of predicting the time of flight utilizing a non-uniform group velocity is outlined. Using this method and the polynomial fits, predictions of time-of-flight of the fundamental antisymmetric mode are made and corroborated with the observed values. Further, to circumvent the need of the prior knowledge of the group velocity variation in predicting the time-of-flight, a generalized expression of the variation of the group velocity is developed by employing the adiabatic nature of the GGW. The present analysis and the proposed methods can find their potential use in the wave-based NDE of tapered HCSS.

1. Introduction

Structures incorporating a thick hexagonal honeycomb core sandwiched between two thin skin panels or face sheets are extensively employed in marine and aerospace industries due to their higher strength, higher stiffness-to-weight ratios, and higher energy-absorption qualities [1–4]. While face sheets offer resistance to in-plane loads, the core enhances the flexural stiffness of the overall structure with minimal weight gain [5]. In spite of their numerous advantages, honeycomb core sandwich structures (HCSSs) are vulnerable to several hidden defects and damage arising out of ageing, impact and intensive loading [6–8]. Therefore, the frequent Non-Destructive-Evaluation (NDE) of sandwich structures for identification, characterization and monitoring of any potential defects or damage [9] is essential.

In the last couple of decades, an umpteen number of research works have proven the applicability and advantages of guided waves (GWs) in detecting and characterizing various defects in structures, such as: plates, pipes, etc. [10–12]. The ability of the

GWs to traverse through the entire thickness of the component and propagate considerably long distances with little energy loss makes them a suitable contender for their use in the emergent NDE techniques [13]. Spurred with the unique advantages of GW-based NDE techniques, increasing number of researchers have explored their application potential in detecting various defects in sandwich structures, lately [14–19]. Some of the recent studies [14,15] have demonstrated the use of GWs for detecting the presence of debond at the skin-core interface. In this regard, the authors of the aforementioned studies have employed changes in the modal amplitudes observed at the sensor location. The literature also reports detection and characterization of debond in HCSS accomplished by employing different GW signal features, such as: time reversal [20], coefficient of signal difference [21] and time-of-flight (ToF) [22], etc. The use of GWs for detecting and characterizing other defects in HCSS, such as: barely visible low-speed impact damage (BVLID) [23,24], high density core [25], etc. has also been demonstrated, numerically as well as experimentally.

In most of the aforementioned studies, frequencies of GWs employed for inspecting sandwich panels are high enough that the GWs propagate only through one side of the face sheet on which the actuator is located. With such high frequencies of the interrogation signal, the energy leaked in the core does not always reach the bottom face sheet to which the actuator is not attached. In addition, the displacement pattern for the whole of the sandwich structure resembles the Rayleigh (surface) waves. However, for the top face sheet, it resembles that of the Lamb waves with a stress-free boundary on top and the other boundary in contact with the thick core, which dissipates the energy before it reaches the other face sheet [15,26]. This, in turn, limits the applicability of these methods to detect the debond like defects that are on the same side of the face sheet-core junction to which the actuator and the sensor are attached [27]. This limitation can be circumvented with the use of low frequency excitation signal that results in the formation of standing wave pattern across the entire thickness of the investigated honeycomb sandwich structure. GWs with such displacement pattern that spans along the entire thickness of sandwich are also referred to as the global GWs (GGWs) [28]. Mustapha et al. [29] have demonstrated the applicability of such low frequency GWs in detecting debond irrespective of the position of the actuator and the sensor. However, the sandwich panel considered by these authors is a flat panel with uniform core thickness. While most of the aforementioned studies pertaining to GW-based NDE of HCSS consider the similar flat structure with constant thickness, those used in the actual marine and aerospace applications have mostly an airfoil shape. The non-uniform thickness of the core used in these sandwich structures gives them the desired airfoil shape. To the best of the authors' knowledge, the investigation of low frequency GW propagation through a sandwich structure whose core thickness is non-uniform and varies continuously in an airfoil shape has not been reported so far in the literature. This forms one of the primary motivations of the present investigation and is addressed numerically as well as experimentally, in the initial part of this article.

Nevertheless, studies exploring the GW propagation though metallic plates with a smooth change in their thickness profile have been reported earlier. In this regard, a handful of researchers [30–32] have delineated that when low-order GW modes encounter a varying thickness waveguide, they propagate as adiabatic modes wherein the energy flux of the propagating wave remains invariant to the change in the thickness. Further, the local properties of the wave (such as wavenumber, group velocity and phase speed) get altered so as to match the local thickness of the waveguide. In one such study, a duraluminium plate with linear thickness variation is numerically and experimentally investigated for the adiabatic behavior of the propagating GW mode by El-Kettani et al. [33]. The wavenumber of the propagating GW modes, as reported by these authors, changes with the varying thickness of the plate, ascertaining the adiabatic nature of the propagating GW mode. The study further demonstrates that the wave properties at any specific position in a varying thickness waveguide are equivalent to that of a constant thickness structure with the corresponding frequency-thickness product. Dispersion properties of the fundamental symmetric (S_0) wave mode that propagates through an aluminium plate with the smooth thickness variation have also been investigated by Hu et al. [34]. Authors of this article have reported the observation of continuous increase in the phase velocity and continuous reduction in the wavenumber of the GW mode as it propagates along the direction of thickness reduction.

As demonstrated by the aforementioned literature references, the continuous and smooth change in the waveguide thickness results in the continuous variation of wave properties such as wavenumber, phase speed and group velocity. By carrying out systematic numerical and experimental investigations, the current manuscript demonstrates that the aforementioned adiabatic behavior of the GWs is also observed for HCSS with non-uniform and smoothly varying core thickness. On the experimental front, piezoelectric transducer (PZT) induced GW propagation through a helicopter blade structure made up of an aluminium honeycomb core and glass fibre reinforced polymer (GFRP) composite face sheets is investigated. Whereas, on the numerical front, an equivalent model with tuned damping properties is employed for carrying out the transient wave propagation analysis. Local wave properties, such as: wavenumber, phase speed and group velocity are extracted by processing the displacement responses. Laser Doppler vibrometer (LDV) setup is employed for recording the displacement response of the waveguide on the experimental front. Continuous change in the local wave properties along the thickness reduction direction is reported in this article. The adiabatic nature of the fundamental antisymmetric (A_0) GW mode is thereby established.

The conventional and prevalent ToF based methods employed for defect localization assume constant group velocities of GWs throughout the specimen. However, as reported earlier in case of monolithic plates and demonstrated in the present manuscript for HCSS, the non-uniform and continuous change in the thickness of the waveguide results in the continuous change in group velocity of GWs. The current manuscript presents a method that can accommodate the variation in the group velocity for accurate estimations of time-of-arrival (ToAs) and hence the ToFs of wave packets that can potentially be used in defect detection algorithms for such waveguides. In this regard, initially, the variation in group velocity observed in the chosen waveguide is employed. To make the method more generic and applicable for any thickness profile, local group velocities are then predicted by using dispersion curve of equivalent constant thickness HCSS. Accordingly, the present manuscript addresses the two-fold objective by undertaking the investigation of low frequency ultrasonic GW propagation through HCSS, whose core thickness varies smoothly. At first, the local variations in the GW properties as they propagate through a helicopter blade structure is presented and secondly, a method for
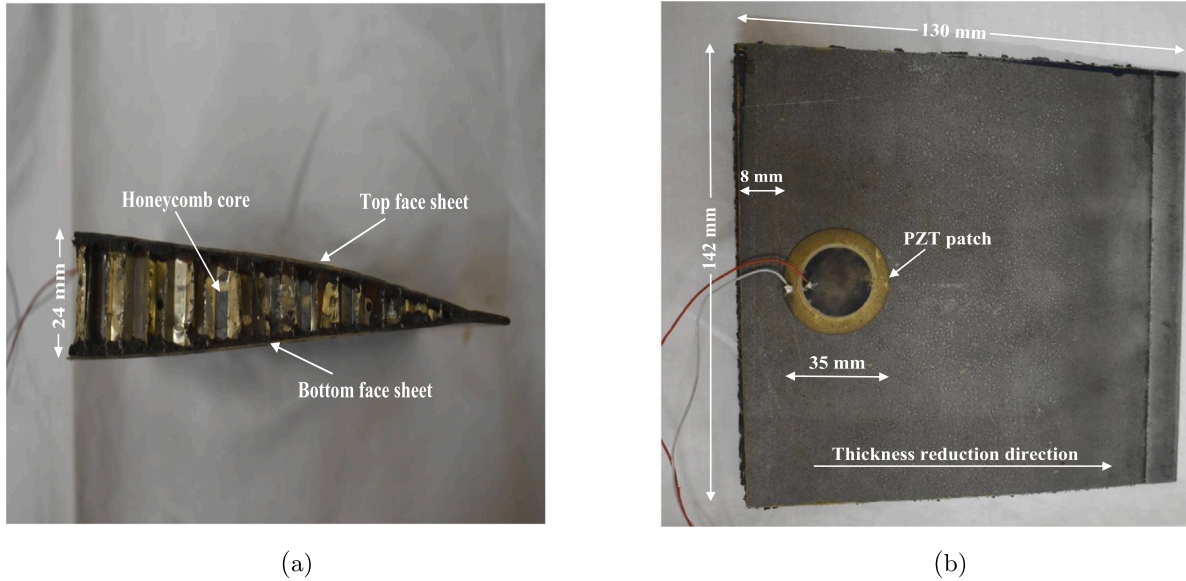
(a)

(b)

Fig. 1. Cross-section (a) and top view (b) of the HCSS specimen used for experimental investigations.

Table 1
Specimen material properties.

For core:									
Material	E (GPa)	v	ρ (kg/m³)						
Aluminium T6061	69	0.33	2700						

For face sheets:									
Material	E_{11} (GPa)	E_{22} (GPa)	E_{33} (GPa)	G_{12} (GPa)	G_{13} (GPa)	G_{23} (GPa)	v_{12}	v_{13}	v_{23}	ρ (kg/m³)
GFRP	44.68	6.9	6.9	2.54	2.54	2.5461	0.28	0.28	0.355	1870

predicting ToAs of low frequency GW signals is presented for HCSS waveguides whose core thickness is non-uniform and varies smoothly.

The remainder of the paper is organized as follows: Section 2 describes the experimental setup in detail, including the procedure for selecting an optimum interrogation frequency for the GW propagation in a helicopter blade specimen made up of a honeycomb sandwich structure. The numerical framework is described in Section 3. In Section 4, the non-uniform dispersive behavior of the propagating GWs is discussed. The numerical and experimental ToA and ToF predictions of different wave packets incorporating the non-uniform group velocity are illustrated in Section 5. Section 6 presents an overview of a generalized method of ToF predictions for a general thickness profile of HCSS. The concluding remarks are presented in Section 7.

2. Experimental procedure

Fig. 1 shows a honeycomb core structure used as a specimen in the experimental investigation. The structure forms a part of helicopter blade, that comprises a couple of thin face sheets (skin panels) attached to a thick honeycomb core, whose thickness varies continuously from left to right (Fig. 1(a)). The plan view of the specimen can be observed in Fig. 1(b). The honeycomb core has a cell size of 8 mm and a wall thickness of 0.1 mm. The thickness of the top as well as bottom face sheet is 0.5 mm, while the overall maximum thickness of the structure is 24 mm. The core is made up of an aluminium alloy T6061 honeycomb, which is adhesively bonded to two GFRP composite skins having a layup configuration of [0/90/90/0]. Table 1 summarizes the material properties for the core and face sheets; in which, E is the Young's modulus, v is the Poisson's ratio, G denotes the shear modulus and ρ represents the density. The subscript index 1 indicates the direction marked as thickness reduction direction in Fig. 1(b).

The experimental studies are performed using Polytec PSV-400 1D scanning LDV, as depicted in Fig. 2. It measures out-of-plane displacements at predefined grid points on the specimen surface. A circular SP5H PZT patch of 35 mm diameter attached to the specimen surface serves as the actuator and generates the GW signal. The PZT patch is driven by a voltage amplifier which gets input from Polytec inbuilt signal generator. The scanning operation is performed point-by-point in the raster form.

Determination of an optimum excitation frequency for the PZT patch is essential for the successful propagation of GWs through a HCSS whose core thickness varies continuously. To this end, the actuator is supplied with a predefined range of frequencies and the output at a specific location is captured. The received signals for different excitation frequencies are scrutinized to compute the maximum displacement response and a frequency-response plot is obtained, as shown in Fig. 3(a). The normalization is carried
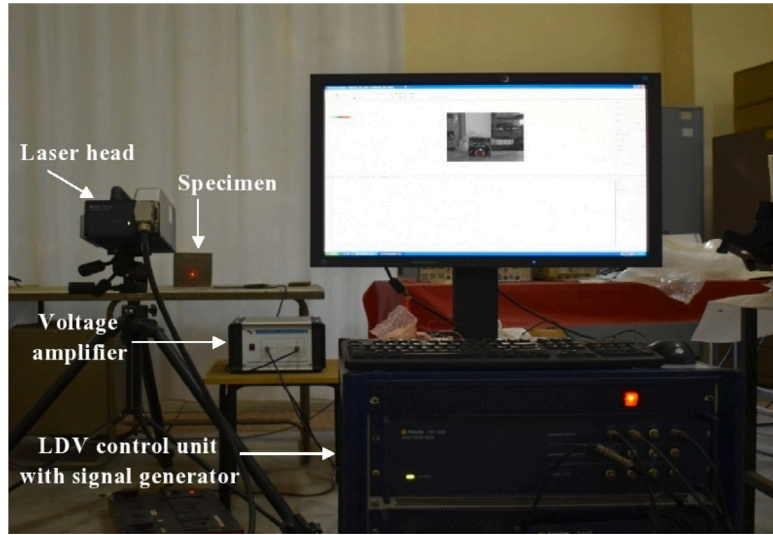
Fig. 2. Experimental setup for the GW propagation in a specimen of honeycomb sandwich structure.
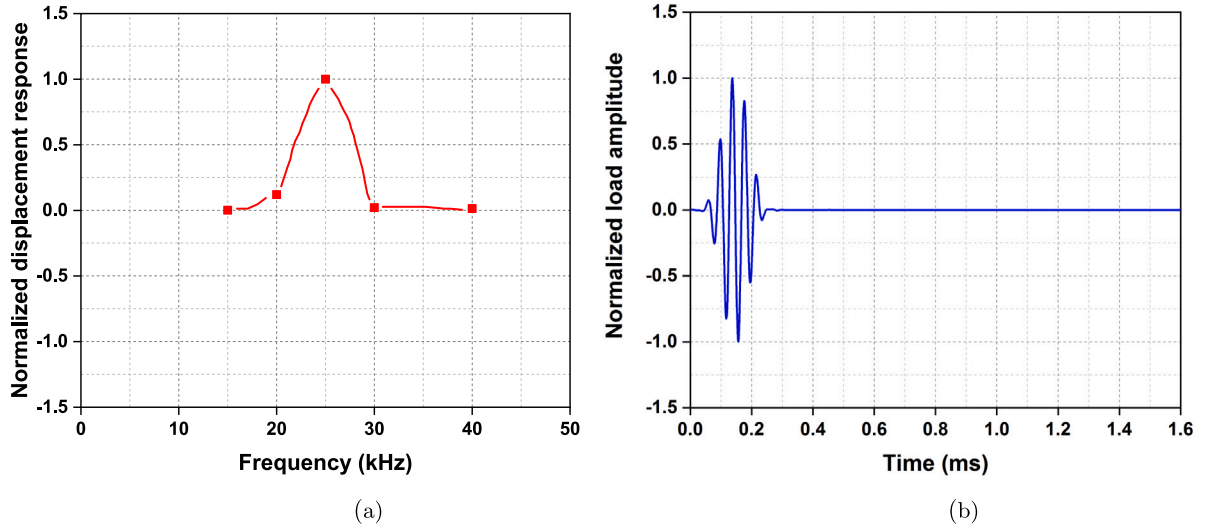

Fig. 3. (a) Variation in maximum displacement amplitude with the central frequency of excitation, indicating the maxima at 25 kHz and (b) the chosen 5-cycle Hann-windowed input pulse with a central frequency of 25 kHz.

out with the peak amplitude of that response where the displacement is observed to be maximum. It is noticed that the actuator shows highest peak in the displacement response at 25 kHz frequency. Thus, a five-cycle Hann-modulated [35] 25 kHz sine pulse represented in Fig. 3(b) is opted for both, the experimental and numerical investigations.

3. Finite element (FE) framework

A three-dimensional (3D) HCSS having a smooth core thickness variation is modeled numerically for investigating the propagation of GWs. In this regard, an equivalent structure with a tapered core (Fig. 4(a)) is considered. For modeling and simulating the GW propagation through this structure, a commercially available FE software, ABAQUS/Explicit is employed. The core and face sheets are bonded using the surface-based tie constraints. These constraints ensure that any relative motion between face sheets and core is nullified. The numerically modeled HCSS with a continuously varying core is illustrated in Fig. 4(a). As shown in Fig. 4(b), the GWs are initiated by employing a set of concentrated loads spread radially [24] throughout a 35 mm diameter circular area created on both the face sheets. Actuation on both sides of the face sheets in numerical model ensures the generation of A_0 mode. However, in the experimental investigations, a single PZT patch is attached on only one face sheet of the specimen. The practical limitation of attaching the other PZT patch at exactly the same location on the bottom face sheet drives this choice. For the chosen frequency and
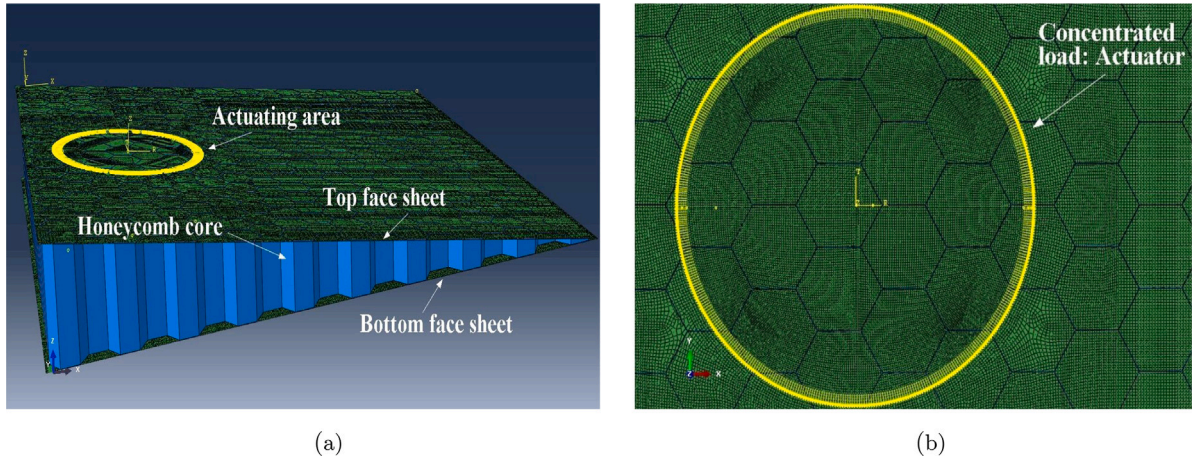
(a)   (b)

Fig. 4. (a) Numerical model of a honeycomb sandwich structure with a smooth core thickness variation (b) modeling of the actuator.
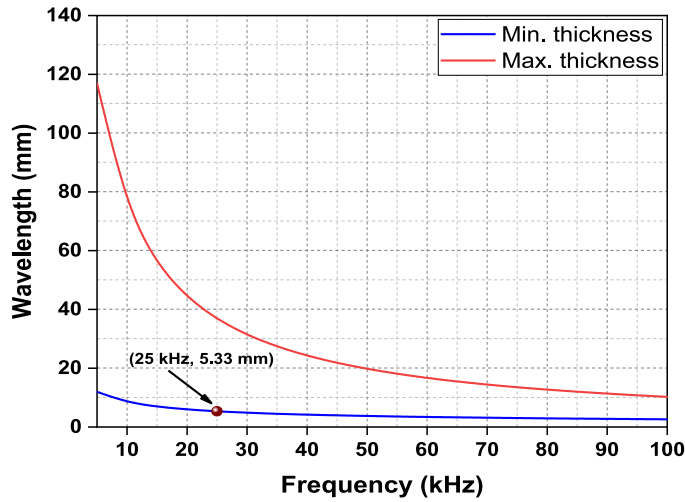

Fig. 5. Wavelength dispersion curve associated with the maximum thickness and minimum thickness of the model.

the actuator, the difference in the actuation methods in experimental and numerical approaches results into very little difference in the generated wavefields, which is evident from an excellent comparison between the numerical and experimental results presented later in this section.

To account for an appropriate spatial resolution, the element size must be fine enough to ensure that at least 20 nodal distance per wavelength exist [36] and which is prescribed by

$$L_e = \frac{\lambda_{\min}}{20},$$ (1)

where, L_e represents the element size and $\lambda_{\min}$ represents the minimum wavelength of the propagating wave. The determination of minimum wavelength necessitates a dispersion curve in a predefined frequency range. To this end, the semi-analytical finite element (SAFE) [37] approach is utilized by taking into account the equivalent homogeneous properties [38] of the core. The dispersion curve for two different model thicknesses highlighting the variation of wavelength with respect to frequency is depicted in Fig. 5. The minimum wavelength at an excitation frequency of 25 kHz corresponding to the minimum thickness of the model is observed to be 5.33 mm. Thus, conforming to Eq. (1), an element size of 0.25 mm has been chosen to discretize the entire numerical model of HCSS. The conventional four-noded quadrilateral S4R shell element having six degrees of freedom at each node has been incorporated to model both the face sheets and core. The finely meshed honeycomb core is depicted in Fig. 6. It should be noted that the homogenized properties of the core are used only for estimating the wavelength and subsequently selecting the minimum element size that is used in the finite element simulations.

The integration step time (Δt) used in simulation is chosen to address the two considerations. Firstly, the sampling frequency (inverse of Δt) should be high enough to capture the wave pattern correctly. This leads to the generation of at least twenty times
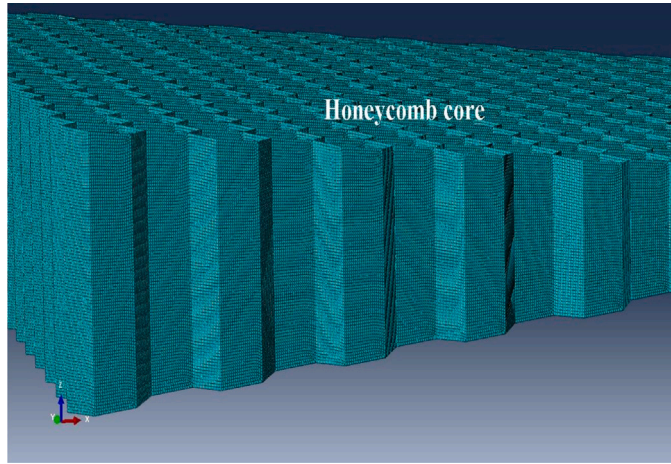
Fig. 6. Mesh discretization of the core.

greater sampling frequency than the highest frequency involved in the analysis [39]. If the maximum frequency of excitation is $f_{\max}$, then

$$\Delta t \leq \frac{1}{(20 f_{\max})}. \tag{2}$$

Secondly, the time step size should satisfy the Courant–Friedrichs–Lewy (CFL) condition [40], the statement of which is as the following:

$$\Delta t \leq \frac{L_{min}}{C_{max}}, \tag{3}$$

in which, L_{min} is the minimum distance between the two nodes and C_{max} is the maximum speed of the wave. In order to address both these constraints, an integration time step size of 0.01 μs is employed in the numerical simulations. The following subsection describes the tuning of numerical framework in order to accomplish a better agreement with the experimental outcomes.

3.1. Tuning of damping properties used in FE framework

To obtain a consistent comparison between the numerical simulations and the experimental observations, it is necessary to model appropriately the dissipation mechanism in the numerical framework. This is particularly important since the face sheets of the sandwich structure are made up of GFRP, which exhibits considerable attenuation. Further, the levels of energy dissipation offered by the face sheets and the core are dissimilar. One of the viable models is the Rayleigh damping model [41], in which the equivalent damping coefficient for the entire sandwich structure is obtained through a combination of the mass proportional (α) and the stiffness proportional (β) damping coefficients. These coefficients should be determined such that the number of prominent peaks as well as the relative amplitudes of the wave packets are consistent in both the numerically obtained and experimentally observed response. For the present case, the values of $\alpha = 8 \times 10^3$ and $\beta = 5 \times 10^{-10}$, respectively represent the optimum values leading to an appreciable match between the two, and hence are chosen in the subsequent analysis. These values of Rayleigh damping parameters are assumed to remain independent of the location and hence are constant throughout the waveguide. The A-scan displacement response at a generic location (60 mm from the circumference of the actuator), recorded experimentally and obtained by the numerical approach is depicted in Fig. 7. A notable agreement between the experimental and numerical result validates the numerical framework, which is then used in the further analysis. The marginal difference in the signals can be attributed to the slight nonconformity existing in the geometry of the structure. The actual structure resembles an airfoil shape whereas the numerical model of HCSS comprises an equivalent linearly varying core thickness.

3.2. Wavefield images

Fig. 7 substantiates the similarity of the results obtained by the numerical and experimental methods at a single point on the waveguide. To ensure that the correlation between the numerical and experimental results holds at other locations on the waveguide, wavefield images for the complete waveguide are obtained by both the experimental and numerical methods. These images are typically the pictorial representation of the out-of-plane displacement response recorded at a particular time instant of 0.166 ms. The experimental and numerical wavefield images with consistent colormaps depicted in Figs. 8(a) and (b), respectively, exhibit a satisfactory correlation between the two. However, the spatial modulation of the wave due to the presence of periodic core is evident from the numerical wavefield image (Fig. 8(b)), and also in the experimental one (represented by a white circle) as shown
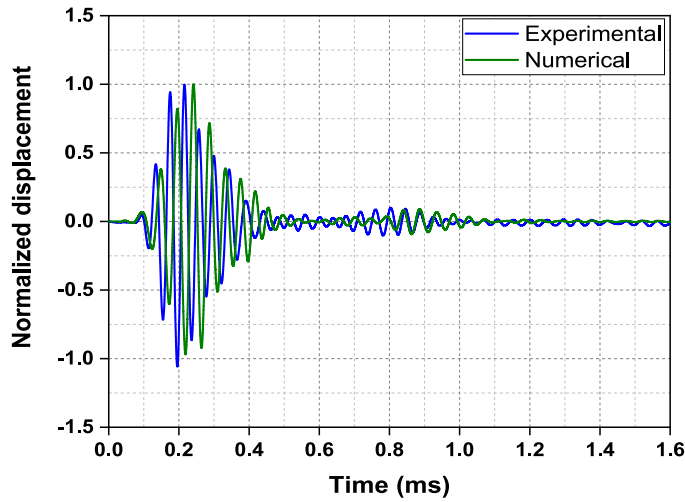
Fig. 7. Comparison of experimental and numerical displacement response at a generic location (60 mm away from the circumference of the actuator along the thickness reduction direction).
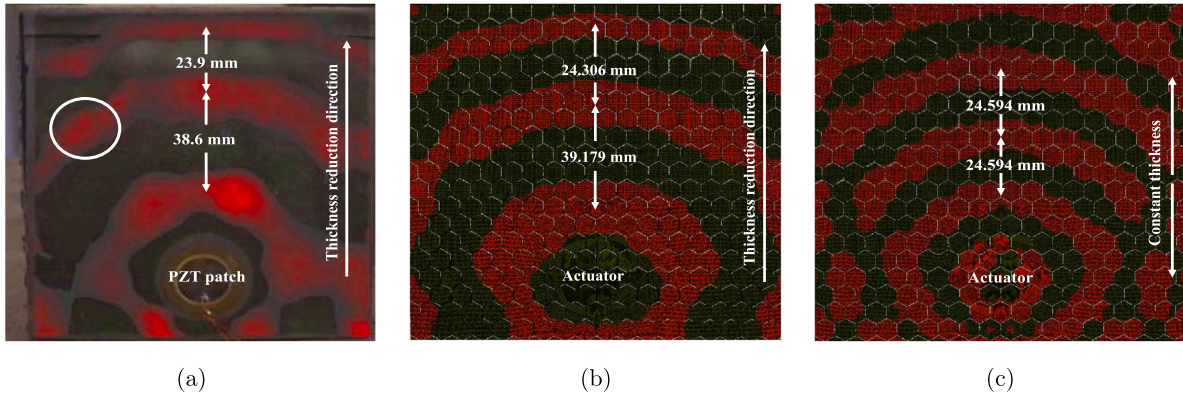

(a)   (b)   (c)

Fig. 8. Wavefield patterns for (a) HCSS with a continuous core thickness variation (Experimental), (b) specimen of HCSS with smooth core thickness variation (Numerical) and (c) HCSS possessing a constant core thickness (Numerical).

in Fig. 8(a). As depicted in the wavefield images (Figs. 8(a) and (b)), the distance between the two successive wavefields is observed to vary along the thickness reduction direction, in both the experimental and numerical results. As stated earlier, a slight difference between the two could be attributed to dissimilar thickness profiles considered in the numerical and experimental analysis. In order to emphasize the role of smooth thickness variation in generating the observed variation in wavefield patterns, a similar image is generated, numerically, for a waveguide whose thickness is constant throughout, and is equal to the average thickness of the waveguide. The wavefield image for the constant thickness waveguide is shown in Fig. 8(c), that depicts a little change in the distance between the wavefield pattern, unlike the other two (Figs. 8(a) and (b)). The following section describes in detail the variations in wave properties observed in Figs. 8(a) and (b) along the thickness reduction direction.

4. Adiabatic GWs and non-uniform dispersion characteristics

As described by Song et al. [28], GWs characterized by the standing wave pattern across the entire thickness of the sandwich structure, generated at a very low frequency of excitation, are designated as the GGWs. Fig. 9 shows the numerically obtained 3D wavefield image of a tapered HCSS excited by a 25 kHz tone burst signal. The magnitude of the out-of-plane displacement at any point on the surface of the structure is represented by the colors, whose values are represented in the adjoining color bar. The confirmation of the propagation of GGW in the HCSS under consideration when excited using a 25 kHz frequency signal is achieved when a standing wave pattern is formed across the entire thickness of the sandwich structure. Towards this, displacements at three peculiar points: on the top face sheet, at the mid-core location and on the bottom face sheet are measured. These three peculiar points are shown in Fig. 9 on which the markings as a, b and c, respectively represent the chosen peculiar points on the top face sheet, mid-core and bottom face sheet, respectively. Displacements measured at three points along the wave propagation directions
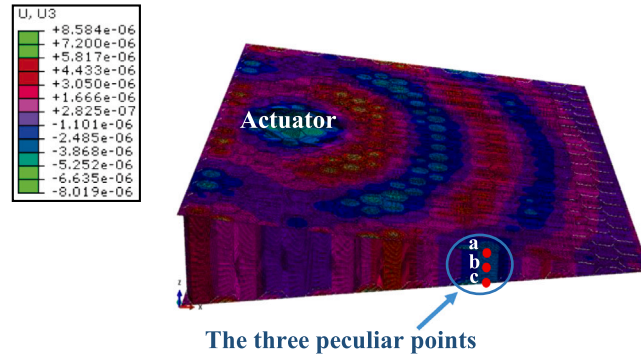
Fig. 9. 3D wavefield image showing the colorscale representation of the out-of-plane displacement at any point on the surface of the structure recorded numerically.
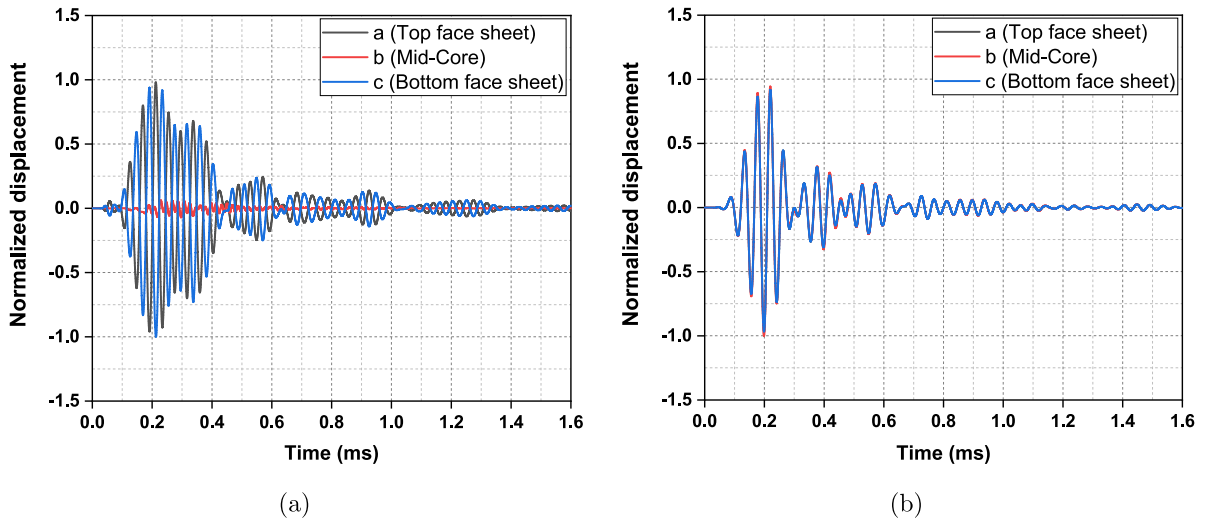

Fig. 10. (a) Out-of-phase behavior of in-plane displacement, and (b) in-phase behavior of out-of-plane displacement.

and in the out-of-plane directions are shown in Figs. 10(a) and (b), respectively. As evident from these figures, displacements in the direction of wave propagation show antisymmetric nature with a 180-degrees phase shift between the top and the bottom points. While the out-of-plane displacements at these three points are exactly in phase and are almost uniform. These figures authenticate the propagation of standing wave pattern across the overall thickness of the HCSS and also ascertain the propagation of the A_0 mode. Previous research efforts, in case of monolithic metallic plates with smooth thickness variations have demonstrated that GWs adapt themselves to the changing thickness of waveguide by altering the local GW characteristics, such as: wavenumber, phase speed, etc. [34]. Wavefield images shown in Figs. 8(a) and (b) also indicate the variations in wave properties when GGWs propagate through HCSS with non-uniform core thickness. In order to further investigate the variations in GWs properties along the thickness reduction direction, local wavenumber, phase speed and group velocity are extracted from the numerically and experimentally obtained displacement responses of the HCSS under consideration.

4.1. Extraction of local GW properties

In order to determine the local wave properties of the propagating GW mode, the time–history responses obtained in the out-of-plane direction using numerical as well as experimental methods are employed. An algorithm used in this regard, is developed in-house that utilizes the cross-correlation technique [42,43]. This technique processes two signals at a time which are recorded at two different points located in the vicinity of the sensing location at which local wave properties are to be computed. The wave property determined by processing these two signals would give the averaged wave property of the investigated sensing location. Now, this process involves an iterative time shifting of one signal against the other, in which one of those two signals is treated as the reference while the other signal undergoes a modification in time and phase to correlate with the baseline signal. The correlation coefficient computed at every iterations attains its maximum when the two cross-correlated signals display the best similarity.
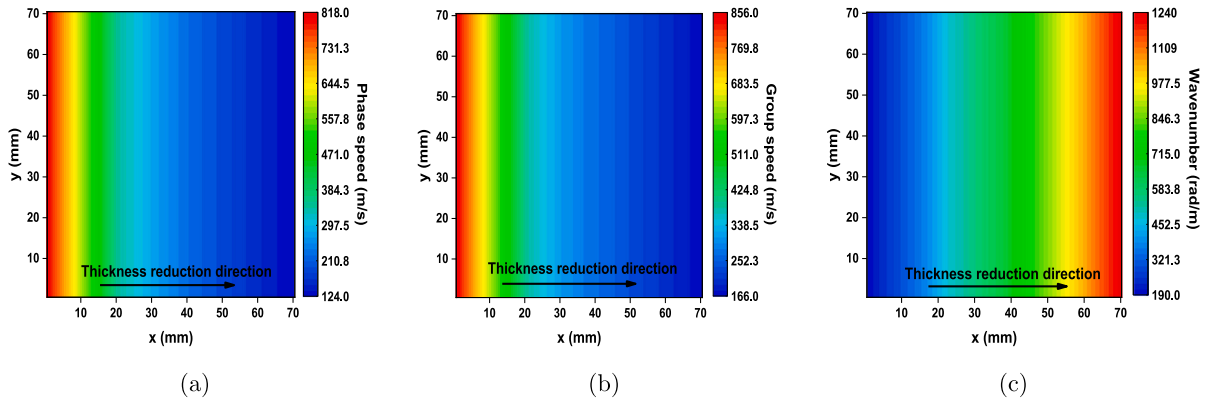
Fig. 11. Variation of (a) phase speed, (b) group speed and (c) wavenumber over the waveguide geometry, obtained by using the numerical results.

The process initiates by determining the wave envelopes of two output signals recorded at two different spatial locations. This is accomplished by taking the magnitude of the Hilbert transform of the two recorded signals, as mentioned in the following:

$$e_1(t) = |H(s_1(t))| \qquad \text{and} \qquad e_2(t) = |H(s_2(t))|, \tag{4}$$

in which, s_1 and s_2 are the two output A-scan responses, whereas, e_1 and e_2 are corresponding wave envelopes. The time delay between the two wave signals is then obtained by the cross-correlation of the envelopes as:

$$t_d = arg\ max((e_1 \star e_2)(\tau)), \tag{5}$$

where, τ is the applied time shift and t_d is the value at which the correlation gets maximized. The phase delay ϕ_0 is then estimated which is based on the maximization of the cross-correlation between $s_2^*(t - t_d)$ and $s_1(t)$. Next, after applying ϕ_0 iteratively to s_2^*, the signals s_1 and s_2^* are cross-correlated and the correlation coefficient with t_d is computed. This iterative process terminates when the correlation coefficient with t_d reaches the maximum that reveals the optimum phase difference, and is defined as:

$$\phi = arg\ max((s_1 \star s_2^*)(t_d)(\phi_0)), \tag{6}$$

where, s_2^* is the signal with a delayed phase shift. Therefore, with a knowledge of the distance between the sensing points, time, phase and excitation frequency, the phase speed, group velocity and the wavenumber can be computed as:

$$C_p = \frac{x}{t_d + \frac{\phi}{\omega}}, \tag{7}$$

$$C_g = \frac{x}{t_d}, \tag{8}$$

$$k = \frac{\omega}{C_p}, \tag{9}$$

where, C_p is the phase speed, C_g represents the group velocity, k is the wavenumber, x is the propagation distance of the wave and ω is the angular frequency of the wave.

A specific number of sensing points from the circumference of the actuator has been chosen for the determination of multiple GW properties and their response towards the continuous core thickness variation of HCSS is illustrated subsequently.

4.2. Response of the GW properties to varying thickness of HCSS

In order to investigate the effect of core thickness variation on the local GW properties, numerically obtained out-of-plane displacements over a grid of equispaced points on the waveguide surface are considered, initially. By employing the method of extracting the wave properties described in Section 4.1, images of wavenumber, phase speed and group speed variation over the waveguide are obtained. The plots shown in Fig. 11 clearly indicate that the local phase speed (C_p), group velocity (C_g) and wavenumber (k) undergo maximum variations along x direction while they remain constant along y. Coordinates x and y are measured from the actuator location.

To further investigate the variations in local wave properties, a few points lying along the x direction that marks the steepest change (Fig. 12) are chosen. Local wave properties at each of the chosen points are determined by employing the out-of-plane displacement responses obtained by the numerical and experimental methods.

The experimental and numerical values of dispersion characteristics of GWs are graphically represented in Fig. 13. Second-order polynomial fit capturing the variations of each of these wave properties with the distance from the actuator as well as the thickness of the waveguide are depicted (Fig. 13). It should be noted that the distance from the actuator has an inverse correlation with
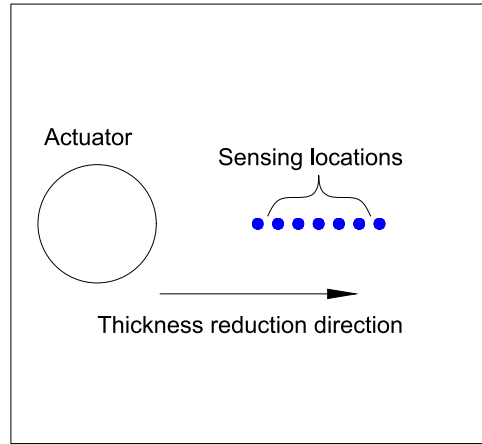
Fig. 12. Schematic of waveguide depicting the grid of equidistant sensing locations.

(a)   (b)
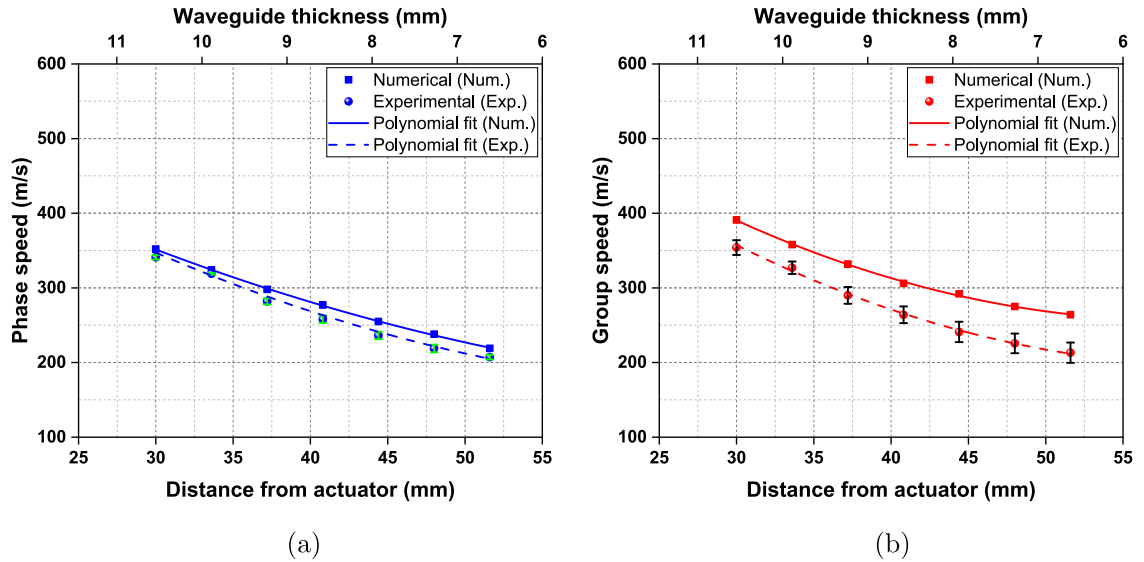
Fig. 13. Numerical and experimental variation of (a) local phase speed and (b) local group velocity in relation to the distance from the actuator and the waveguide thickness.

the thickness of the investigated structure. The phase speed and group velocity are observed to decrease with the increase in the distance from the actuator. The numerical results depict a satisfactory agreement with the experimental outcomes. The standard error bars on the experimentally obtained values are also constructed and provided in the figure (Fig. 13). It is therefore observed that when the core thickness in a honeycomb sandwich structure is continually changing, the local wave properties also undergo a change which substantiates the adiabatic mode of the propagating GW.

5. ToF predictions for GWs with non-uniform group velocity

As mentioned in Section 1, the primary motivation behind executing this study, apart from investigating the A_0 mode's adiabatic nature, is to develop a prospective framework for GW-based damage detection in a real-life HCSS that does not have a constant thickness profile. The existing GW-ToF based methods that are used for damage detection (discussed in Section 1) are mostly concerned with the constant thickness waveguides and hence are based on the assumption of the uniform group velocity. However, Section 4.2 has demonstrated that the GW dispersion properties at low frequency range are not constant in HCSS waveguide whose core thickness in non-uniform. The present section outlines a method that can predict the ToFs of the aforementioned low frequency GGW modes by taking into account the non-uniform group velocity variations.

To this end, the ToA of three peculiar A_0 mode wave packets at a few arbitrarily selected sensing locations along the taper axis are considered for prediction. These three wave packets arrive at the sensing location by following three peculiar paths that are
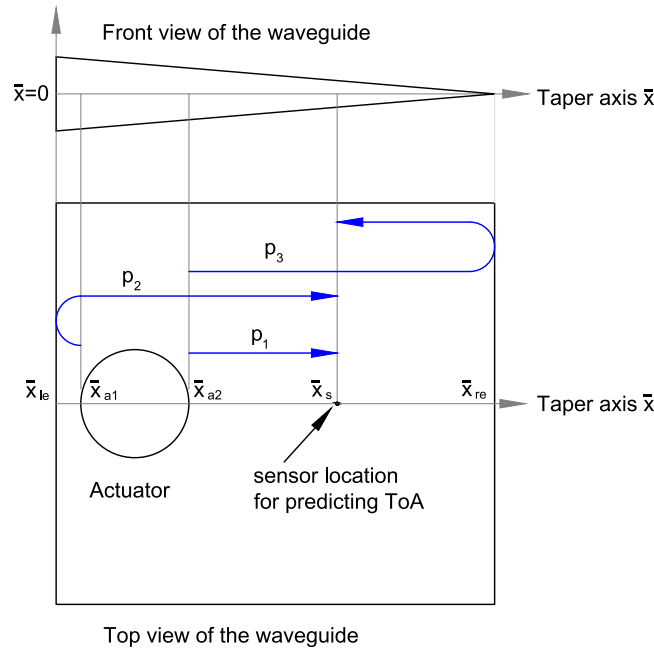
Fig. 14. Schematic representation of different paths traversed by the GW lobes whose ToAs at the sensor location are predicted.

depicted schematically in Fig. 14. The first path p_1 starts from actuator and ends directly at the sensor, in the shortest route. The peak of the wave packet following this path is assumed to arrive at the sensor location at time t_1. The second wave packet under consideration, traverses along path p_2, starting from the actuator to the left edge of the structure and then reflects back without mode conversion. While the peak of the second wave packet is assumed to arrive at time t_2 at the sensor, that of the third and the last lobe under consideration is assumed to appear at t_3. The latter of the two represents a wave packet of A_0 mode that travels along path p_3 from the actuator to the right edge and finally reflecting back to the sensor.

The ToA (t_i) of the aforementioned ith lobe at the sensor location is determined as:

$$t_i = t_a + t_{f_i},$$ (10)

in which, the term t_a is the peak time of wave at the actuator location and t_{f_i} is the ToF of the A_0 mode wave packet traveling along the ith path. In order to estimate the ToF (t_{f_i}), the known variation of group velocity of A_0 mode along the taper axis of the waveguide is employed. Fig. 15 depict the variations of C_g with the distance of measuring point from the actuator that are obtained respectively by experimental and numerical methods. The second-order interpolation functions mentioned in Fig. 15 are obtained as the best polynomial fit to the data points that capture the variations of the group velocity with the distance from the actuator. The variable x stated in the inset of the figure measures the distance of sensing location from the actuator circumference in mm. For facilitating ToF predictions, the independent variable x stated in these polynomial fit functions (Fig. 15) is changed to the location of the cross-section along the taper axis ($\bar{x}$). Fig. 14 also depicts this taper axis.

The group velocity variations in terms of $\bar{x}$ are then written respectively in case of numerical and experimental investigations as:

$$Cg = 164425\bar{x}^2 - 33381.55\bar{x} + 1951.024 \quad \text{and} \quad Cg = 171590\bar{x}^2 - 35446.74\bar{x} + 2030.109.$$ (11)

Note that the unit of $\bar{x}$ used while arriving at the group velocity expressions stated in Eq. (11) is meters. While arriving at the interpolation functions stated in Eq. (11), local group velocities at a few points lying between the actuator and the right end of the waveguide are considered, which are depicted in Fig. 12. Assuming that these variations of group velocity remain unchanged throughout the entire waveguide, they are used for predicting the ToFs that A_0 mode would take to travel along the three identified paths. Following are the expressions for ToFs in terms of C_g:

$$t_{f1} = \int_{p_1} \frac{1}{C_g} d\bar{x} = \int_{\bar{x}_{a2}}^{\bar{x}_s} \frac{1}{C_g(\bar{x})} d\bar{x},$$

$$t_{f2} = \int_{p_2} \frac{1}{C_g} d\bar{x} = \int_{\bar{x}_{a1}}^{\bar{x}_{le}} \frac{1}{C_g(-\bar{x})} d\bar{x} + \int_{\bar{x}_{le}}^{\bar{x}_s} \frac{1}{C_g(\bar{x})} d\bar{x},$$ (12)

$$t_{f3} = \int_{p_3} \frac{1}{C_g} d\bar{x} = \int_{\bar{x}_{a1}}^{\bar{x}_{re}} \frac{1}{C_g(\bar{x})} d\bar{x} + \int_{\bar{x}_{re}}^{\bar{x}_s} \frac{1}{C_g(-\bar{x})} d\bar{x}.$$
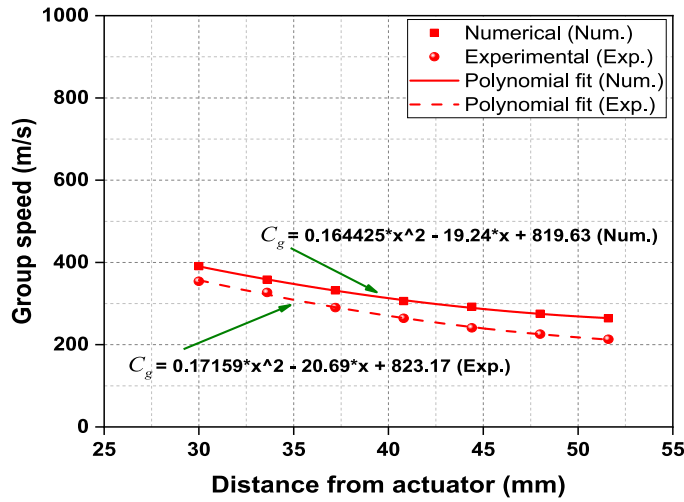
Fig. 15. Variation in local group velocity in relation to distance from the actuator obtained experimentally and numerically.

The term $C_g(-\bar{x})$ mentioned in the aforementioned Eq. (12), represents the group velocity variation in the negative direction of the taper axis $(-\bar{x})$. This is used for predicting ToF for the wave packets that travel along $-\bar{x}$ direction. For example, the wave packet traveling along the path p_2 (Fig. 14) starts from the actuator and travels initially to the left end of the waveguide along the negative direction of the taper axis. Path p_3 also comprises a stretch that involves wave travel along the $-\bar{x}$ direction. Group velocity expressions used for evaluating ToF along these stretches of paths are obtained by replacing the variable $\bar{x}$ stated in Eq. (11) by $-\bar{x}$.

For establishing the accuracy of the method in predicting the ToA of GWs, three different sensor locations are chosen, that are 35 mm, 42 mm and 45 mm away from the actuator along the positive direction of taper axis. Therefore, the cross-sectional locations along the taper axis $(\bar{x})$ that contain the chosen sensing points are 78 mm, 85 mm and 88 mm, respectively. The aforementioned Eq. (12) are then used for obtaining the forecast of ToAs and ToFs at each of the sensing locations. Towards this, the A-scan displacement plots at each of the three chosen sensor locations are shown in Figs. 16(a–c), together with the envelopes that are marked green. The predicted arrival times of three peaks of concern are marked on these graphs using dashed red lines. The actual peaks of the curve that envelopes the displacement signal are also marked on each of these figures with continuous blue lines. The excellent match between the actual and anticipated values is apparent in Figs. 16(a–c).

The similar exercise is carried out employing the experimentally obtained group velocity variation that is shown in Fig. 15. The sensing locations at which the predictions are carried out are maintained at the same distance from the left end of the waveguide, as in case of numerical investigations. The A-scan image of the displacement responses recorded experimentally at each of these sensing locations are depicted in Figs. 16(d–f). Markings of actual peak arrival times and their forecast are also shown in Figs. 16(d–f).

Table 2 encapsulates the numerically and experimentally predicted ToFs obtained by employing the variation of C_g that fits the numerical and experimental data. The numerically and experimentally obtained actual ToFs are also illustrated in that table.

6. ToF predictions for waveguides with generalized thickness variations

The aforementioned discussion established the accuracy of ToF estimations for a specific HCSS, whose core thickness varies in a tapered manner. The method is developed using the known variation of the group velocity along the waveguide. If the same method is to be applied for any other HCSS with a different core thickness profile, it would be necessary to estimate the group velocity variation in that specific waveguide. The following discussion, in this regard, describes a generalized method that can accommodate any thickness profile of HCSS. Some of the previous studies addressing the adiabatic nature of GWs in monolithic plates have demonstrated that local dispersion properties of GWs at any cross section are equivalent to that of constant thickness waveguide with identical frequency-thickness product. In light of this inference, a group velocity dispersion curve is obtained for constant thickness HCSS with identical material and geometric properties, except the thickness profile. The excitation frequencies are varied in a specific range that would cover the required frequency-thickness product range. Fig. 17 shows the group velocity variation over the chosen range of frequency and thickness product.

Fig. 17 also shows the curve that fits the group velocity data extracted from the numerical analysis of the constant thickness HCSS. Expression of the curve in terms of the frequency-thickness product is

$$Cg = 0.005842 f^2 h^2 - 1.195 f h + 298.4, \tag{13}$$

where, f represents the excitation frequency in kHz and h is the waveguide thickness measured in mm. The previously published literature has shown that GWs adapt to the local thickness by changing the wave properties such that the dispersion curve is followed. Assuming that this inference prevails for the HCSS as well, the local group velocity at any cross-section of HCSS can be obtained
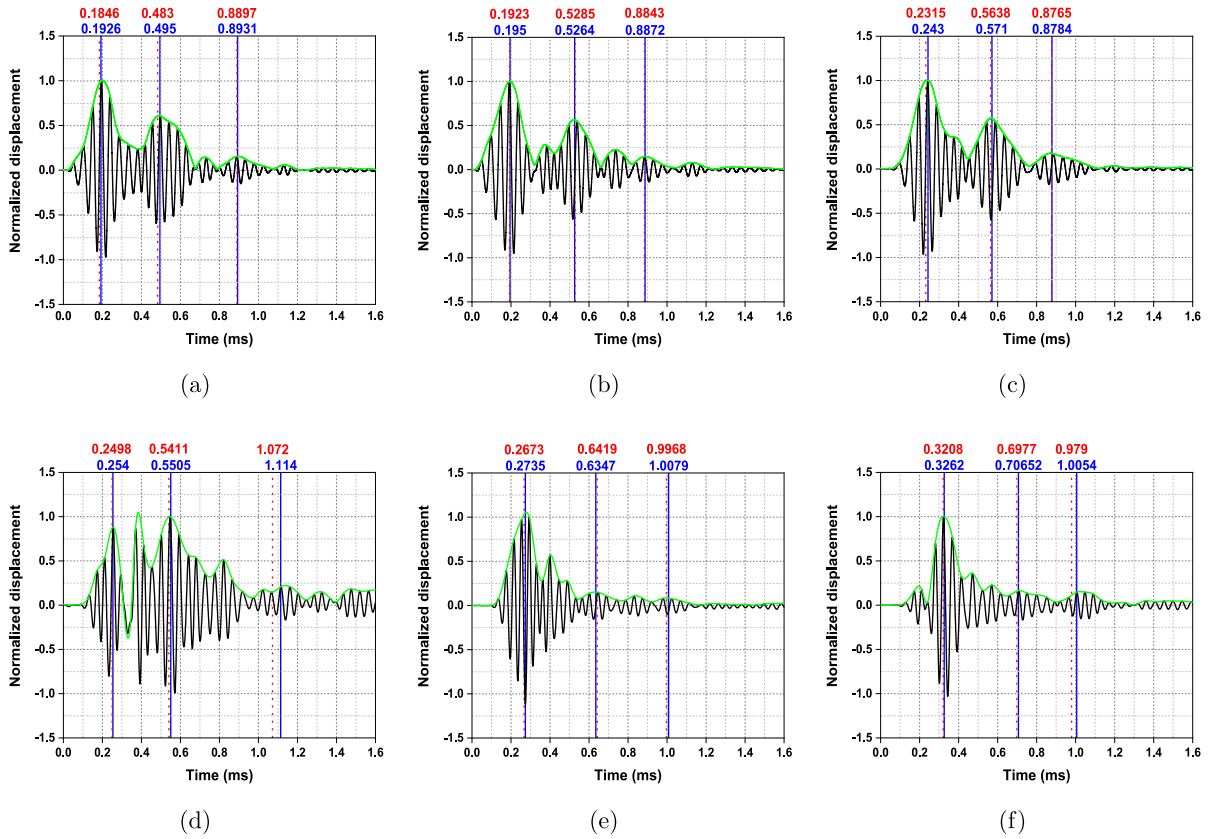
Fig. 16. A-scan displacement responses at three sensing locations that are 78 mm (a,d), 85 mm (b,e), and 88 mm (c,f) away from the left end of the waveguide along the taper axis (Fig. 14), together with the predicted and actual arrival times recorded numerically (a–c) and experimentally (d–f).

Table 2
Predicted and actual values of ToFs of different GW lobes at various reception points (numerical (num.) and experimental (exp.)).

	$\bar{x}_s = 0.078$ m			$\bar{x}_s = 0.085$ m			$\bar{x}_s = 0.088$ m		
	$i = 1$	$i = 2$	$i = 3$	$i = 1$	$i = 2$	$i = 3$	$i = 1$	$i = 2$	$i = 3$
Pred. t_{f_i} (num.)	0.0866	0.385	0.7917	0.0943	0.4305	0.7863	0.1335	0.4658	0.7785
Act. t_{f_i} (num.)	0.094	0.397	0.795	0.097	0.4284	0.7892	0.145	0.473	0.7804
Pred. t_{f_i} (exp.)	0.1061	0.3974	0.9283	0.1236	0.4982	0.8531	0.1771	0.554	0.8353
Act. t_{f_i} (exp.)	0.1103	0.4068	0.9703	0.1298	0.491	0.8633	0.1825	0.5628	0.8612

by knowing the thickness change profile. This is achieved by employing the relationship between the waveguide thickness and the cross-sectional location. For example, in case of the chosen HCSS with a tapered core, the relationship between the core thickness (measured in mm) and cross-section location along the taper axis (measured in m) can be written as:

$$h = 24(1 - \frac{\bar{x}}{0.13}). \tag{14}$$

Using the expression of thickness stated in Eq. (14), the group velocity variation stated in Eq. (13) can be written in terms of $\bar{x}$ as:

$$Cg = 122727\bar{x}^2 - 26483.52\bar{x} + 1665.5639. \tag{15}$$

The expression of C_g in terms of $\bar{x}$ can then be employed for determining the ToFs and ToAs, as mentioned in Section 5. The only change in this method when compared with the one described in Section 5 is in the expression of C_g. While the method described in Section 5 used the expression of C_g that was obtained by processing the GW signals propagating through the tapered waveguide (Eq. (11)), the generalized method described in this section employs the expression of C_g (Eq. (15)) obtained by the using the dispersion curve of constant thickness HCSS and the thickness profile information. The predicted ToAs and those observed in numerical A-scan displacement responses at the three investigated sensing locations are shown in Figs. 18(a–c). An excellent match between the predicted (red dashed lines) and actual values (blue continuous lines) at all three reception points displayed in Figs. 18(a–c), validates the framework.
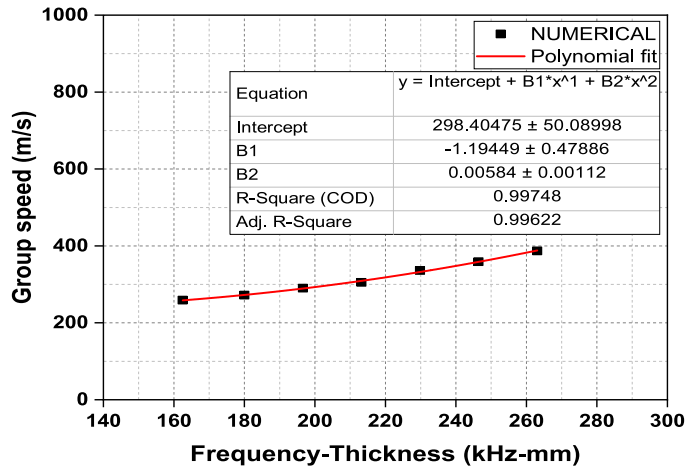
Fig. 17. Constant thickness group velocity dispersion curve (Numerical).

Table 3

Predicted and actual values of ToFs of different GW lobes at various reception points (numerical (num.) and experimental (exp.)). Predictions are based on the C_g expression obtained by employing the group velocity dispersion curve for a constant thickness HCSS together with the expression of the respective thickness profile.

	$\bar{x}_s = 0.078$ m			$\bar{x}_s = 0.085$ m			$\bar{x}_s = 0.088$ m		
	$i = 1$	$i = 2$	$i = 3$	$i = 1$	$i = 2$	$i = 3$	$i = 1$	$i = 2$	$i = 3$
Pred. t_{f_i} (num.)	0.0889	0.3867	0.7896	0.0956	0.4319	0.7851	0.1359	0.4683	0.7781
Act. t_{f_i} (num.)	0.094	0.397	0.795	0.097	0.4284	0.7892	0.145	0.473	0.7804
Pred. t_{f_i} (exp.)	0.1072	0.3967	0.9323	0.1254	0.4935	0.8536	0.1753	0.5501	0.8455
Act. t_{f_i} (exp.)	0.1103	0.4068	0.9703	0.1298	0.491	0.8633	0.1825	0.5628	0.8612

The validated generalized method is further employed for predicting the ToFs and ToAs of GWs in the actual helicopter blade structure that is used as a specimen in the experimental approach. The blade structure used in the experiments has an airfoil cross-section. The expression of the cross-sectional thickness of the HCSS at any location along the taper axis is not linear but follows the relation stated in the following [44]:

$$h = 10 h_{max} c [0.2969(\frac{\bar{x}}{c})^{0.5} - 0.126(\frac{\bar{x}}{c}) - 0.3516(\frac{\bar{x}}{c})^2 + 0.2843(\frac{\bar{x}}{c})^3 - 0.1015(\frac{\bar{x}}{c})^4], \qquad (16)$$

where, h_{max} denotes the maximum thickness and c represents the chord length.

The expression of C_g in terms of $\bar{x}$ is then obtained by replacing variable h appearing in Eq. (13) with the thickness expression stated in Eq. (16). The resultant expression of C_g is then used for evaluating ToF predictions stated in Eq. (12). The predicted values of ToA along with the experimentally recorded ones are marked on the experimental A-scan responses illustrated in Figs. 18(d–f). The predicted values correlates well with the observed values and is apparent in Figs. 18(d–f).

The predicted and actual values of ToFs of different GW lobes at various reception points computed numerically and experimentally using the C_g expression for constant core thickness HCSS display an excellent match, and are listed in Table 3.

7. Conclusions

The low frequency antisymmetric GW propagation through a HCSS whose thickness profile is non-uniform is analyzed numerically and experimentally. The specimen used for the experimental investigations is a part of an actual helicopter blade structure, comprising two thin GFRP face sheets and an aluminium honeycomb core whose thickness reduces smoothly to give it an airfoil shape. An equivalent numerical model, but with a linear taper core, is analyzed for GW propagation using commercial FE software. Surface-mounted PZTs are used for generating low frequency ultrasonic GWs in the experimental analysis, whereas an equivalent point-force method is employed in numerical investigations. Rayleigh damping is used for modeling the dissipation characteristics. The mass and stiffness proportionality constants used in this damping model are obtained by tuning the numerically obtained displacement response with that observed in the experiments. The wavefield patterns for the entire waveguide are obtained by employing the tuned FE framework on the numerical front and by using scanning LDV on the experimental front. An excellent comparison between the experimental and numerical results validates the numerical framework.

Two important observations are recorded from the resultant wavefield patterns, that are: (1) formation of the standing wave across entire thickness of HCSS and (2) progressive change in the wavefields along the taper axis of the waveguide. The former observation establishes the generation of GGWs, while the latter indicates the adiabatic nature of the GWs. In order to further
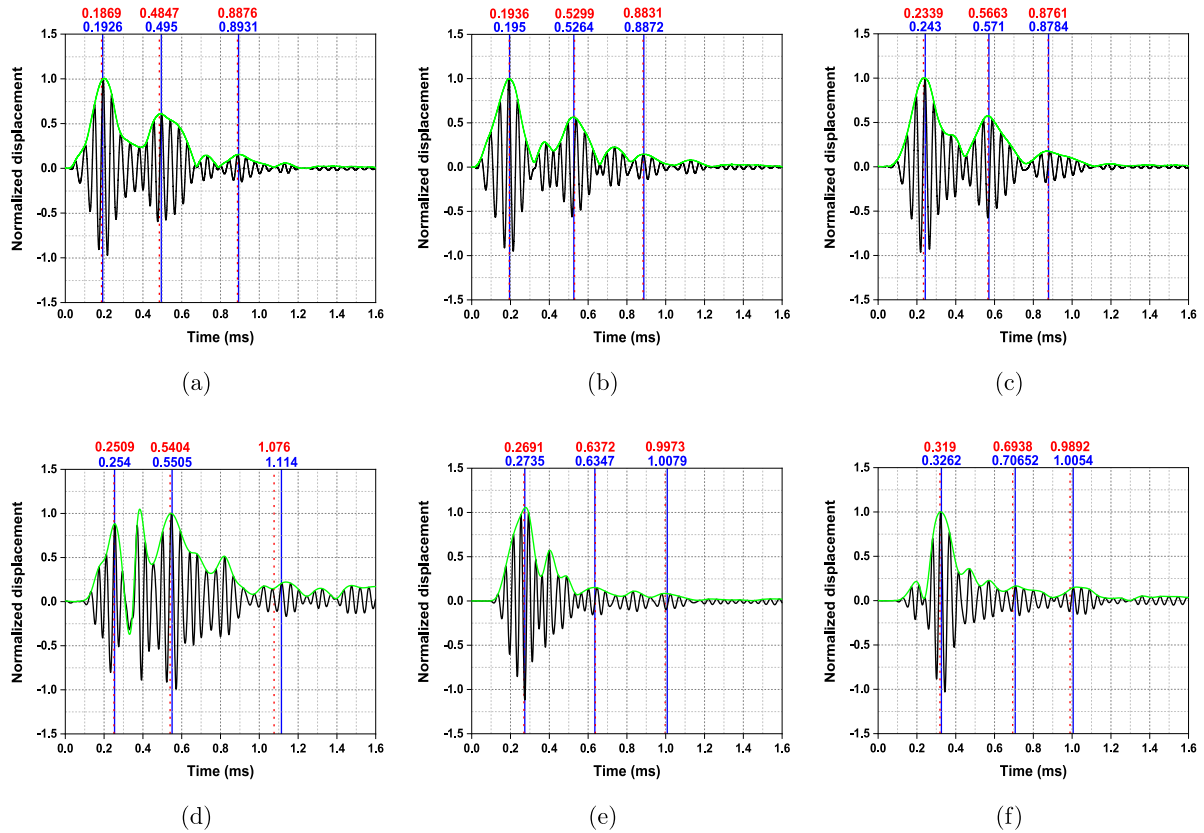
Fig. 18. A-scan displacement responses at three sensing locations that are 78 mm (a,d), 85 mm (b,e), and 88 mm (c,f) away from the left end of the waveguide along the taper axis (Fig. 14), together with the predicted and actual arrival times recorded numerically (a–c) and experimentally (d–f).

substantiate the claim of the adiabatic nature of the GWs, local wave properties, such as: wavenumber, phase speed and group velocity are obtained by processing the displacement responses recorded numerically as well as experimentally. The results indicate non-uniform distribution of these wave properties along the taper axis of the waveguide.

In light of the non-uniform group velocity variations along the taper axis of the waveguide, a method for predicting ToFs of A_0 GW modes is presented for facilitating potential defect localization algorithms that can be applied for such waveguides. In this regard, a priori known group velocity variation along the GW propagation path is employed, which is obtained by processing the displacement responses. An excellent comparison of predicted and observed values of ToFs and ToAs on both numerical and experimental fronts establishes the method's accuracy. In order to circumvent the need of a priori known group velocity variation and for accommodating any thickness profile of waveguide, a further refinement is presented. To this end, the local group velocity profile is obtained by using the adiabatic nature of low frequency GGWs. In this regard, GWs are assumed to follow the dispersion curve of an equivalent constant thickness HCSS, such that wave properties at any cross-section are equivalent to that in case of constant thickness HCSS with the corresponding frequency-thickness product. The applicability of the method is demonstrated by predicting the ToFs and ToAs for the chosen HCSS. For the purpose of demonstration, GW signals considered for predicting ToFs and ToAs are the reflected waves from the edges of defect-free HCSS. However, the same method can be employed for predicting ToFs of signals that are scattered from the defects, which can then be used for defect localization/imaging.

Declaration of competing interest

The authors declare that they have no known competing financial interests or personal relationships that could have appeared to influence the work reported in this paper.

Data availability

Data will be made available on request.

Acknowledgments

References

[1] J. Fatemi, M. Lemmen, Effective thermal/mechanical properties of honeycomb core panels for hot structure applications, J. Spacecr. Rockets 46 (3) (2009) 514–525.

[2] F. Zhu, G. Lu, D. Ruan, Z. Wang, Plastic deformation, failure and energy absorption of sandwich structures with metallic cellular cores, Int. J. Prot. Struct. 1 (4) (2010) 507–541.

[3] V. Birman, G.A. Kardomateas, Review of current trends in research and applications of sandwich structures, Compos. B Eng. 142 (2018) 221–240.

[4] N. San Ha, G. Lu, X. Xiang, Energy absorption of a bio-inspired honeycomb sandwich panel, J. Mater. Sci. 54 (8) (2019) 6286–6300.

[5] E. Oterkus, C. Diyaroglu, D. De Meo, G. Allegri, Fracture modes, damage tolerance and failure mitigation in marine composites, in: Marine Applications of Advanced Fibre-Reinforced Composites, Elsevier, 2016, pp. 79–102.

[6] X. Zhao, H. Gao, G. Zhang, B. Ayhan, F. Yan, C. Kwan, J.L. Rose, Active health monitoring of an aircraft wing with embedded piezoelectric sensor/actuator network: I. Defect detection, localization and growth monitoring, Smart Mater. Struct. 16 (4) (2007) 1208.

[7] V. Giurgiutiu, G. Santoni-Bottai, Structural health monitoring of composite structures with piezoelectric-wafer active sensors, AIAA J. 49 (3) (2011) 565–581.

[8] J. Chiachío, M. Chiachío, S. Sankararaman, A. Saxena, K. Goebel, Condition-based prediction of time-dependent reliability in composites, Reliab. Eng. Syst. Saf. 142 (2015) 134–147.

[9] T.R. Hay, L. Wei, J.L. Rose, T. Hayashi, Rapid inspection of composite skin-honeycomb core structures with ultrasonic guided waves, J. Compos. Mater. 37 (10) (2003) 929–939.

[10] D.G. Luchinsky, V. Hafiychuk, V.N. Smelyanskiy, S. Kessler, J. Walker, J. Miller, M. Watson, Modeling wave propagation and scattering from impact damage for structural health monitoring of composite sandwich plates, Struct. Health Monit. 12 (3) (2013) 296–308.

[11] C.M. Yeum, H. Sohn, J.B. Ihn, H.J. Lim, Instantaneous delamination detection in a composite plate using a dual piezoelectric transducer network, Compos. Struct. 94 (12) (2012) 3490–3499.

[12] F. He, Z. Zhou, Z. Feng, Research on an inspection method for de-bond defects in aluminum skin-honeycomb core sandwich structure with guided waves, in: 17th World Conference on Nondestructive Testing, Citeseer, 2008, pp. 25–28.

[13] M. Moix-Bonet, D. Schmidt, P. Wierach, Structural health monitoring on the SARISTU full scale door surround structure, in: Lamb-Wave Based Structural Health Monitoring in Polymer Composites, Springer, 2018, pp. 463–473.

[14] S. Sikdar, S. Banerjee, Identification of disbond and high density core region in a honeycomb composite sandwich structure using ultrasonic guided waves, Compos. Struct. 152 (2016) 568–578.

[15] C. Schaal, A. Mal, Core-skin disbond detection in a composite sandwich panel using guided ultrasonic waves, J. Nondestruct. Eval., Diagn. Progno. Eng. Syst. 1 (1) (2018).

[16] S. Mustapha, L. Ye, Damage identification and assessment in tapered sandwich structures using guided waves, in: Key Engineering Materials, Vol. 558, Trans Tech Publ, 2013, pp. 25–38.

[17] S. Sikdar, J. Pal, Bag of visual words based machine learning framework for disbond characterisation in composite sandwich structures using guided waves, Smart Mater. Struct. 30 (7) (2021) 075016.

[18] Y. Lugovtsova, J. Bulling, O. Mesnil, J. Prager, D. Gohlke, C. Boller, Damage quantification in an aluminium-CFRP composite structure using guided wave wavenumber mapping: Comparison of instantaneous and local wavenumber analyses, NDT E Int. 122 (2021) 102472.

[19] P. Fiborek, P. Kudela, Model-assisted guided-wave-based approach for disbond detection and size estimation in honeycomb sandwich composites, Sensors 21 (24) (2021) 8183.

[20] S. Mustapha, L. Ye, Propagation behaviour of guided waves in tapered sandwich structures and debonding identification using time reversal, Wave Motion 57 (2015) 154–170.

[21] F. Song, G. Huang, G. Hu, Online guided wave-based debonding detection in honeycomb sandwich structures, AIAA J. 50 (2) (2012) 284–293.

[22] K. Diamanti, C. Soutis, J. Hodgkinson, Lamb waves for the non-destructive inspection of monolithic and sandwich composite beams, Compos. Part A-Appl. S. 36 (2) (2005) 189–195.

[23] S. Sikdar, P. Kudela, M. Radzieński, A. Kundu, W. Ostachowicz, Online detection of barely visible low-speed impact damage in 3D-core sandwich composite structure, Compos. Struct. 185 (2018) 646–655.

[24] S. Mustapha, L. Ye, X. Dong, M.M. Alamdari, Evaluation of barely visible indentation damage (BVID) in CF/EP sandwich composites using guided wave signals, Mech. Syst. Signal Process. 76 (2016) 497–517.

[25] S. Sikdar, S. Banerjee, Guided wave propagation in a honeycomb composite sandwich structure in presence of a high density core, Ultrasonics 71 (2016) 86–97.

[26] S. Mustapha, L. Ye, Leaky and non-leaky behaviours of guided waves in CF/EP sandwich structures, Wave Motion 51 (6) (2014) 905–918.

[27] X. Qi, J.L. Rose, C. Xu, Ultrasonic guided wave nondestructive testing for helicopter rotor blades, 2008.

[28] F. Song, G. Huang, K. Hudson, Guided wave propagation in honeycomb sandwich structures using a piezoelectric actuator/sensor system, Smart Mater. Struct. 18 (12) (2009) 125007.

[29] S. Mustapha, L. Ye, D. Wang, Y. Lu, Assessment of debonding in sandwich CF/EP composite beams using A0 Lamb wave at low frequency, Compos. Struct. 93 (2) (2011) 483–491.

[30] J. Moll, Damage localization in composite structures with smoothly varying thickness based on the fundamental antisymmetric adiabatic wave mode, Ultrasonics 71 (2016) 111–114.

[31] J. Arnold, L. Felsen, Coupled mode theory of intrinsic modes in a wedge, J. Acoust. Soc. Am. 79 (1) (1986) 31–40.

[32] V. Galanenko, On coupled modes theory of two-dimensional wave motion in elastic waveguides with slowly varying parameters in curvilinear orthogonal coordinates, J. Acoust. Soc. Am. 103 (4) (1998) 1752–1762.

[33] M.E.-C. El-Kettani, F. Luppé, A. Guillet, Guided waves in a plate with linearly varying thickness: experimental and numerical results, Ultrasonics 42 (1–9) (2004) 807–812.

[34] Z. Hu, Z. An, Y. Kong, G. Lian, X. Wang, The nonlinear S0 Lamb mode in a plate with a linearly-varying thickness, Ultrasonics 94 (2019) 102–108.

[35] S. Sikdar, W. Ostachowicz, Ultrasonic Lamb wave-based debonding monitoring of advanced honeycomb sandwich composite structures, Strain 55 (1) (2019) e12302.

[36] M.R. Naserabadi, S. Sodagar, Ultrasonic high frequency Lamb waves for evaluation of plate structures, Acoust. Phys. 63 (4) (2017) 402–409.

[37] A. Marzani, E. Viola, I. Bartoli, F.L. Di Scalea, P. Rizzo, A semi-analytical finite element formulation for modeling stress wave propagation in axisymmetric damped waveguides, J. Sound Vib. 318 (3) (2008) 488–505.

[38] J.R. Vinson, R.L. Sierakowski, The Behavior of Structures Composed of Composite Materials, Vol. 105, Springer, 2006.

[39] A.K. Mitra, A.A. Aradhye, D.M. Joglekar, Adiabatic guided wave propagation through a honeycomb composite sandwich structure with smoothly varying core thickness, 2021.

[40] G. Linga, O. Møyner, H.M. Nilsen, A. Moncorgé, K.-A. Lie, An implicit local time-stepping method based on cell reordering for multiphase flow in porous media, J. Comput. Phys.: X 6 (2020) 100051.

[41] D. Xiao, T. He, X. Liu, Y. Shan, H. Yu, Efficient simulation of acoustic emission with reflections removal based on infinite element and Rayleigh damping, in: ASME International Mechanical Engineering Congress and Exposition, Vol. 56437, American Society of Mechanical Engineers, 2013, V014T15A013.

[42] B. Hernandez Crespo, C.R. Courtney, B. Engineer, Calculation of guided wave dispersion characteristics using a three-transducer measurement system, Appl. Sci. 8 (8) (2018) 1253.

[43] J. Semmlow, Signals and Systems for Bioengineers: A MATLAB-Based Introduction, Academic Press, 2011.

[44] NACA airfoil series, 2001, URL: http://www.aerospaceweb.org/question/airfoils/q0041.shtml.